Volume 18 | Number 1 | 7 January 2016 | Pages 1–636

# PCCP

Physical Chemistry Chemical Physics
www.rsc.org/pccp

ISSN 1463-9076

PERSPECTIVE
Darya Radziuk and Helmuth Möhwald
Ultrasonically treated liquid interfaces for progress in cleaning and separation processes

175 YEARS

This is an Accepted Manuscript, which has been through the Royal Society of Chemistry peer review process and has been accepted for publication.

Accepted Manuscripts are published online shortly after acceptance, before technical editing, formatting and proof reading. Using this free service, authors can make their results available to the community, in citable form, before we publish the edited article. We will replace this Accepted Manuscript with the edited and formatted Advance Article as soon as it is available.

You can find more information about Accepted Manuscripts in the author guidelines.

Please note that technical editing may introduce minor changes to the text and/or graphics, which may alter content. The journal's standard Terms & Conditions and the ethical guidelines, outlined in our author and reviewer resource centre, still apply. In no event shall the Royal Society of Chemistry be held responsible for any errors or omissions in this Accepted Manuscript or any consequences arising from the use of any information it contains.

ROYAL SOCIETY OF CHEMISTRY

rsc.li/pccp

# Formation of Ordered Mesostructured TiO$_2$ Thin Film: A Soft Coarse-Grained Simulation Study

Qiyun Tang* and Marcus Müller

*Universität Göttingen, Institut für Theoretische Physik,*

*Friedrich-Hund-Platz 1, 37077 Göttingen, Germany*

Paula C. Angelomé

*Gerencia Quimica, Centro Atomico Constituyentes,*

*Comision Nacional de Energia Atomica, CONICET,*

*Av. Gral Paz 1499, B1650KNA San Martín, Buenos Aires, Argentina*

Galo J. A. A. Soler-Illia

*Instituto de Nanosistemas Universidad Nacional de General San Martín,*

*CONICET, Av. 25 de Mayo 1021 1650 San Martín, Buenos Aires, Argentina*

**Physical Chemistry Chemical Physics Accepted Manuscript**

# Abstract

Ordered mesostructured $TiO_2$ thin films are employed in diverse applications ranging from catalysis and sensing, to photovoltaic and lithium-ion batteries. Experimentally these mesostructured thin films are fabricated via a sol-gel process coupled with evaporation-induced self-assembly of a supramolecular template, where the concentration of hydrogen chloride (HCl) and water play vital roles. We employ a soft, coarse-grained model of the amphiphilic template Brij58 and spherical particles, representing titanium-oxo clusters, to study the role of HCl and water on the formation of mesostructured $TiO_2$ thin films. The template-cluster and cluster-cluster interactions are reflected in the interaction terms $\delta N_{BP}$ and $\varepsilon_{PP}$, respectively. The results show that the decrease of HCl (increase of $\varepsilon_{PP}$) leads to the formation of large mesopores due to the strong attraction between particles, giving rise to a high dispersity index (low order) of the thin films. However, the decrease of water (increase of $\delta N_{BP}$) will compensate the entropic attraction between particles, resulting in thin films with low dispersity index (high order). The variation of the dispersity index in the $\delta N_{BP}$-$\varepsilon_{PP}$ plane provides an intuitive understanding that the slow evaporation of HCl could drive the film towards uniform mesoporous state whereas fast evaporation pushes the film through a non-uniform phase. These results indicate that even if the mass proportion of the surfactants Brij58 and titanium precursors is the same in the initial solution, the final mesoporous structures could be diverse, which was confirmed by the controlled experiments. We also confirm the post-processing-towards-order strategy by making the particle's rearrangement available by weakening the $\varepsilon_{PP}$. The outlined procedure paves the way of soft, coarse-grained models to understand the complex co-assembly of transition metal clusters and amphiphilic surfactants towards the rational design of highly ordered mesoporous structures.

$^*$ E-mail: qiyun.tang@theorie.physik.uni-goettingen.de

## I. INTRODUCTION

Mesostructured $TiO_2$ materials have found promising applications in catalysis, sensing, photovoltaic, lithium-ion batteries, and are central for energy applications in solar cells and solar fuels [1–4]. Among the various applications of $TiO_2$ materials, mesoporous thin films are of significant importance [5–10].

Often these mesostructured thin films are fabricated by the so-called Evaporation-Induced Self-Assembly process (EISA) [11–16], which implies the combination of a sol-gel process coupled with the self-assembly of a supramolecular template. An initial solution, comprised of Titanium precursors, amphiphilic surfactants, and co-solvents (e.g., HCl and water), is typically dip- or spin-coated onto a substrate (e.g., silicon wafer, fused silica, or glass). The amphiphilic surfactants (such as PEO-based block copolymers Brij56, Brij58, Pluronic P123, or F127) are employed as structure-directing agents (SDA) that self-assemble, and then also co-assemble with the titanium precursors upon drying, leading to ordered mesostructures [2, 7]. The evaporation of co-solvents gradually concentrates the solution, initializing and synchronizing the self-assembly of the surfactants and the condensation of titanium precursors. A detailed analysis of the titanium-oxo-SDA mesophase formation mechanism, based on spectroscopy, mass spectrometry and in situ SAXS led to propose that the co-assembly of the titanium precursors and amphiphilic surfactants initiates after the freshly deposited films has approached the drying line. At this point, most of the co-solvent has evaporated and, subsequently, the film thickness remains nearly constant. As time progresses, the residual HCl and water gradually evaporate. Mass-spectroscopy experiments demonstrate that the evaporation rate of HCl is slower than that of water [14]. The time-dependent concentrations of co-solvents modulate the condensation ability of titanium precursors and interaction between the precursors and PEO blocks [17, 18]. After treating the freshly obtained mesostructure and removing the surfactants, one eventually obtains mesoporous $TiO_2$ thin films that can present different degrees of ordering [19].

The key feature of this fabrication strategy consists in controlling two kinetic processes that take place in parallel: the self-assembly of the SDA upon solvent evaporation, and the fast hydrolysis and condensation rates of the titanium precursor [2, 7]. While the first process can be controlled through external synthesis variables such as the solvent, the atmosphere in which the film is deposited, or a post treatment procedure, Ti(IV) condensation can

be controlled through a low-pH environment [18], stabilizing ligands [20, 21], nonaqueous media [22, 23], preformed nanoclusters [17, 24], and "acid-base pairs" (titanium alkoxide mixed with $TiCl_4$) [25, 26].

The most extended synthesis route implies the use of titanium chloride in ethanol-water solutions, or titanium alkoxides in highly acidic media; both conditions imply an important concentration of HCl. During the formation of mesostructured $TiO_2$ thin films, the hydrogen chloride (HCl) and water play different but important roles:

The acid HCl, generated *in situ* or added, is an efficient inhibitor for the condensation reaction between titanium precursors [18]. However, during the evaporation of ethanol/$H_2O$/HCl, the concentration of HCl, and thus the acidity of the deposited film, varies. In the initial titanium precursor solution, the concentration of $H^+$ is sufficiently high to prevent the fast condensation of titanium precursors. Upon approaching the drying line, the residual concentration of $H^+$ still remains high due to the pronounced decrease of film thickness in the early stage of evaporation. This effect was confirmed by X-ray Absorption Spectroscopy (XAS) and mass spectrometry of freshly deposited films [14], which indicate the low condensation ability of titanium clusters. As the co-assembly of the surfactant and titanium precursors progresses, however, the residual HCl gradually evaporates and the titanium clusters condense together into ordered mesostructures.

Water also tunes the interaction between PEO-based surfactants and titanium clusters [17]. In non-protic solvents, in the absence of water, there is a strong binding between PEO monomers and Ti(IV) molecular or cluster species due to the transalcoholysis and chelation caused by coordination bonds between the titanium center and the PEO blocks [27]. However, upon water addition, the strong chelation interactions are replaced by relatively weak dipolar or hydrogen-bond interaction, forming hydrophilic titanium clusters [13, 14, 17]. Additionally, in anhydrous environment (such as organic solvent ethanol), the repulsion between the hydrophilic PEO and hydrophobic blocks of the amphiphilic surfactants is rather small, which prevents the formation of well ordered mesostructures. Upon adding water, this repulsion between the blocks increases, yielding more ordered mesostructures. This solubility difference of the blocks also can be effectively increased by the formation of hydrophilic titanium clusters upon addition of water, as discussed previously. Moreover, the existence of water can also promote the hydrolysis-condensation reactions between titanium clusters [18]. However, this effect can be compensated by the inclusion of inorganic acids,

such as HCl. These distinct crossed effects illustrate the complex role of water on the formation of ordered mesostructured TiO$_2$ thin films.

While the complex modulation of the chemistry as a function of the concentration of HCl and water has been investigated rather thoroughly from the experimental point of view, and the time-dependence of the co-solvent concentrations in the course of the fabrication process has been exploited to control the final material, the correlation between the two factors and the physical properties of the final mesostructured TiO$_2$ thin films, such as the size distribution and the order of the formed mesopores, is only incompletely understood. In addition, advanced applications such as mesoporous (photo)catalysts, solar cells or separation membranes would greatly benefit from a model that establishes a sound base to pre-design relevant materials features, such as mesopore size and spatial organization, which depend not only in the intrinsic SDA size, but also in the complex kinetics implicated in thin film deposition, drying and processing.

Here we devise a coarse-grained model that allows us to explore the role of the concentration of HCl and water on the mesostructure formation. In this exploratory approach, we explicitly model the titanium precursors and surfactants that build the final mesostructured TiO$_2$ thin film but integrate out the degrees of freedom of the co-solvents. The titanium precursors are represented by small, spherical nanoparticles (NPs) [28] and the PEO-based surfactant, Brij58, by a soft, bead-spring model of an AB diblock copolymer [29]. Within our implicit-solvent model, the effect of the concentration of HCl and water is qualitatively represented through the interactions between the titanium precursors and surfactants. In accord with experimental studies discussed above, HCl chiefly modulates the strength, $\varepsilon_{PP}$, of attraction between nanoparticles (NPs), whereas water additionally affects the affinity, $\delta N_{BP}$, between the PEO-based copolymers and the titanium-oxo clusters. This coarse-grained modeling approach allows us to access the large time and length scales of the fabrication process and to systematically investigate the dependence on the co-solvent-induced interactions.

Our paper is organized as follows: In the next section, we describe the modeling and simulation techniques of the PEO-based surfactant Brij58 and titanium-oxo clusters. In Sec. III, we study the influence of the interaction strengths, $\varepsilon_{PP}$ and $\delta N_{BP}$, on the size distribution of the mesopores and the variation of the dispersity index. We also show that the structural dispersity can be reduced by post-processing. Subsequently, we discuss the

ability of our coarse-grained simulation to understand the formation of mesostructured $TiO_2$ thin films, and compare it to the simulations of the nanocomposites of block copolymers and NPs. The manuscript concludes with a brief summary and outlook.

## II.  MODEL AND SIMULATION TECHNIQUE

### A.   A soft, coarse-grained model for titanium clusters and Brij58

We consider $n$ amphiphilic surfactants and $n_P$ nanoparticles in a volume $V$ with periodic boundary conditions at a constant temperature $T$.

The PEO-based surfactant, H-$[CH_2CH_2]_8$-$[OCH_2CH_2]_{20}$-OH, which we denote in the following by Brij58, is represented by a bead-spring model with soft, non-bonded interactions [29]. This top-down model incorporates bonded interactions that describe the linear chain architecture and non-bonded interactions that give rise to microphase separation in the surfactant solution.

The molecular contour is discretized into $N$ beads. Neighboring beads along the molecular backbone are connected by harmonic springs

$$\frac{\mathcal{H}_b[\{\mathbf{r}_{i,s}\}]}{k_B T} = \sum_{i=1}^{n} \sum_{s=1}^{N-1} \frac{3(N-1)}{2R_{e0}^2}[\mathbf{r}_{i,s+1} - \mathbf{r}_{i,s}]^2 \tag{1}$$

where $\mathbf{r}_{i,s}$ with $i = 1, \cdots, n$ and $s = 1, \cdots, N$ denotes the coordinate of the $s^{\text{th}}$ bead on surfactant $i$. $R_{e0}$ denotes the end-to-end distance of the chain molecules in the absence of non-bonded interactions.

The amphiphilic surfactant, Brij58, is comprised of 8 hydrophobic ethyl repeat units -$[CH_2CH_2]$- and 20 hydrophilic PEO repeating units -$[CH_2CH_2O]$-. Ignoring the volume difference of the two bead species, we roughly estimate the hydrophobic volume fraction of the surfactant, $f_A = 8/28$. In our computational model, we discretize the chain contour into $N = 40$ coarse-grained beads with a similar hydrophobic fraction as Brij58, i.e., each amphiphile is represented by $A_{12}B_{28}$. The end-to-end distance of Brij58 can be roughly estimated as $R_{e0} \approx R_e = 3.96$ nm, where we ignore the small difference between model parameter, $R_{e0}$, and the end-to-end distance, $R_e$, in a melt.

The mass density of Brij58 is 1.018 g/cm$^3$ with the molecular weight of 1123 g/mol. Thus the number density of Brij58 is $\rho_0 N \simeq 906$mol/m$^3$. These values result in a square

root of the invariant degree of polymerization, $\sqrt{\mathcal{N}} = \rho_0 R_{e0}^3/N \simeq 34$. i.e., the number of amphiphiles is given by $n = \sqrt{\mathcal{N}}V/R_{e0}$.

During the EISA process, the inclusion of HCl in the titanium precursor solutions inhibits the fast condensation of precursors [30]. According to small angle X-ray scattering measurements [31, 32], titanium-oxo subunit clusters of approximate size 2 nm are the nano building blocks for the co-assembly process that ensues after passing the drying line. Therefore we model these titanium-containing subunit clusters as spherical NPs. These NPs interact via a Lennard-Jones potential

$$
\frac{U_{PP}(r)}{k_B T} = \varepsilon_{PP}\Big[\Big(\frac{\sigma_{PP}}{r}\Big)^{12} - \Big(\frac{\sigma_{PP}}{r}\Big)^{6} \\
- \Big(\frac{\sigma_{PP}}{r_{\text{cut}}}\Big)^{12} + \Big(\frac{\sigma_{PP}}{r_{\text{cut}}}\Big)^{6}\Big]
$$
(2)

where $r$ denotes the distance between the particle centers. This interaction between NPs defines their shape and size. The diameter of the spherical NPs is $\sigma_{PP} = 0.668R_{e0} \approx 2.6$ nm. The Lennard-Jones potential is cut-off and shifted to zero at the distance $r_{\text{cut}} = 1.5R_{e0} = 2.2455\sigma_{PP}$, i.e, beyond the minimum at $r_{\min} = 2^{1/6}\sigma_{PP}$. The strength of NP attraction, $\varepsilon_{PP}$, tailors the condensation ability between the modeled titanium clusters.

The other non-bonded interactions are catered for by an excess free-energy functional of the local normalized densities of hydrophobic and hydrophilic beads and NPs, $\phi_A(\mathbf{r})$, $\phi_B(\mathbf{r})$, and $\phi_P(\mathbf{r})$, respectively. Here the local microscopic $A$ density $\phi_A(\mathbf{r})$ is defined as:

$$
\phi_A(\mathbf{r}|\{\mathbf{r}_{i,s}\}) = \frac{1}{\rho_0}\sum_{i=1}^{n}\sum_{s=1}^{N}\gamma_{i,s}\delta(\mathbf{r} - \mathbf{r}_{i,s}).
$$
(3)

where $\gamma_{i,s} = 1$ if the $s$th segment is of type $A$ and 0 otherwise. A similar expression holds for the microscopic $B$ density. The density of nanoparticles is defined as $\phi_P(\mathbf{r}) = \sum_{i=1}^{n_p}\theta(|\mathbf{r}-\mathbf{r}_i|)$ with

$$
\theta(d) = \begin{cases} 1, & d < R_{\text{core}} \\ \frac{1}{2}\Big(1 + \cos\Big[\frac{(d-R_{\text{core}})\pi}{\xi}\Big]\Big), & R_{\text{core}} \leq d \leq R_{\text{core}} + \xi \\ 0, & d > R_{core} + \xi, \end{cases}
$$
(4)

where $R_{\text{core}} = 0.3R_{e0}$ and $\xi = 0.15R_{e0}$ denote the core radius of the NP and the width of its surface, respectively. We note that the width of the surface region between the NP and

the amphiphiles is rather broad. In our model, this width of the spherical NP qualitatively accounts the rather irregular shape of the titanium-oxo subunits, that have been generated by sol-gel processing [30] and is independent from the environment.

The densities are employed to compute the remaining non-bonded interactions between the segments of the amphiphiles and the NPs. The first term accounts for the limited compressibility of the liquid comprised of amphiphiles and NPs

$$\frac{\mathcal{H}_{\mathrm{nb}}^{\mathrm{comp}}}{k_B T} = \sqrt{\overline{\mathcal{N}}} \int \frac{\mathrm{d}\mathbf{r}}{R_{e0}^3} \frac{\kappa N}{2} [\phi_A(\mathbf{r}) + \phi_B(\mathbf{r}) + \phi_P(\mathbf{r}) - 1]^2 \tag{5}$$

where $\kappa N$ is proportional to the inverse isothermal compressibility. In our simulations we use the value $\kappa N = 80$.

The second contribution describes the repulsion between the hydrophobic and hydrophilic beads of the amphiphile

$$\frac{\mathcal{H}_{\mathrm{nb}}^{AB}}{k_B T} = -\sqrt{\overline{\mathcal{N}}} \int \frac{\mathrm{d}\mathbf{r}}{R_{e0}^3} \frac{\chi N}{4} [\phi_A(\mathbf{r}) - \phi_B(\mathbf{r})]^2 \tag{6}$$

where the combination, $\chi N$, of Flory-Huggins parameter and number of beads per molecule parameterizes the repulsion between the two blocks of the amphiphiles that gives rise to microphase separation. Since the HCl and water are integrated out in our soft coarse-grained model, also the pH only has minor influence on the effective repulsion between the two blocks of Brij58, its influences on the phase behaviour of Brij58 could be effectively incorporated into the parameter $\chi N$. In the simulation we use the value $\chi N = 30$ that suffices to introduce microphase separation of the structure-directing agent (SDA). Here we do not expect a pronounced change of the effective Brij58 interactions in the course of structure formation, the $\chi N$ value remains constant.

The third contribution that controls the interaction between the NPs and amphiphiles takes a similar form

$$\frac{H_{\mathrm{nb}}^{AB-P}}{k_B T} = \sqrt{\overline{\mathcal{N}}} \int \frac{\mathrm{d}\mathbf{r}}{R_{e0}^3} \left\{ -\frac{\delta N_{AP}}{4} [\phi_A(\mathbf{r}) - \phi_P(\mathbf{r})]^2 + \frac{\delta N_{BP}}{4} [\phi_B(\mathbf{r}) - \phi_P(\mathbf{r})]^2 \right\} \tag{7}$$

Here $\delta N_{BP} > 0$ controls the magnitude of attractive interaction between NPs and the hydrophilic block of the amphiphiles, representing the affinity between the hydrophilic titanium

clusters and PEO [27]. As discussed above, this affinity depends on the water concentration during the co-assembly process. As the residual water evaporates, the affinity between the titanium clusters and the PEO blocks increases from hydrogen bonding to strong chelation interactions. A positive value of $\delta N_{AP} = 50$, in turn, gives rise to a repulsion between NPs and hydrophobic A blocks.

TABLE I: Parameters used in the simulation

| parameter | value | parameter | value |
|---|---|---|---|
| $\chi N_{AB}$ | 30 | $\sqrt{\overline{\mathcal{N}}}$(Brij58) | 34 |
| $\delta N_{AP}$ | 50 | $N$ | 40=12+28 |
| $\delta N_{BP}$ | $50, \cdots, 80$ | $f_A$ | 0.3 |
| $\kappa N$ | 80 | $\delta R$ | $0.01 R_{e0}$ |
| $\varepsilon_{PP}$ | $1.0, \cdots, 19.0$ | $R_{PP}$ | $0.45 R_{e0}$ |
| $\sigma_{np}$ | $0.668 R_{e0}$ | $R_{\text{core}}$ | $0.30 R_{e0}$ |
| system size | $9.6 \times 9.6 \times 1.2 R_{e0}^3$ | grid   $n_P$ | $192 \times 192 \times 24$   210 |

These densities are computed on a collocation grid [29] with cell size $\Delta L$. Each cell is identified by its index $\mathbf{c}$. The local microscopic density of $A$ segments on cell $\mathbf{c}$, $\phi_A(\mathbf{c})$, is defined as

$$\phi_A(\mathbf{c}) \;=\; \int \frac{d\mathbf{r}}{\Delta L^3} \Pi(\mathbf{c},\mathbf{r})\phi_A(\mathbf{r}) = \frac{1}{\rho_0 \Delta L^3} \sum_{i,s=1}^{n,N} \Pi(\mathbf{c},\mathbf{r}_{i,s}). \tag{8}$$

where the assignment function $\Pi(c,\mathbf{r})$ is normalized

$$\sum_c \Pi(\mathbf{c},\mathbf{r}) = 1 \;\; \forall \mathbf{r} \quad \text{and} \quad \int d\mathbf{r}\Pi(c,\mathbf{r}) = \Delta L^3 \;\; \forall c \tag{9}$$

Here we choose the first-order assignment function:

$$\Pi_{(1)}(\mathbf{c},\mathbf{r}) = \prod_{\alpha \in \{x,y,z\}} \pi(|\mathbf{c}_\alpha - \mathbf{r}_\alpha|) \tag{10}$$

with

$$\pi(d) = \begin{cases} 1 - \dfrac{|d|}{\Delta L}, & \text{for} \quad |d| \leq \Delta L \\[2mm] 0, & \text{otherwise} \end{cases} \tag{11}$$

For the density of NPs, we can also define a function $\Lambda(\mathbf{c}, \mathbf{r})$ to assign the NP density from the continuous space $\phi_P(\mathbf{r})$ onto the grid-based space $\phi_P(\mathbf{c})$ by

$$\phi_P(\mathbf{c}) = \int d\mathbf{r}\Lambda(\mathbf{c}, \mathbf{r})\phi_P(\mathbf{r}) = \sum_{i=1}^{n_p} \int d\mathbf{r}\Lambda(\mathbf{c}, \mathbf{r})\theta(|\mathbf{r} - \mathbf{r}_i|). \tag{12}$$

To directly relate the NP position $\mathbf{r}_i$ to the cell position $\mathbf{c}$, the simplest way is by choosing the assignment function of $\Lambda(\mathbf{c}, \mathbf{r}) = \delta(\mathbf{c} - \mathbf{r})$. Then the NP density on cell $\mathbf{c}$ is obtained by:

$$\phi_P(\mathbf{c}) = \sum_{i=1}^{n_p} \theta(|\mathbf{c} - \mathbf{r}_i|). \tag{13}$$

This completes the description of the model. Unless stated explicitly otherwise, we employ the simulation parameters that are compiled in Tab. I.

## B. Behavior of a single titanium cluster

To illustrate the assignment of the NPs onto the collocation grid and study the role of the different interaction parameters, we first present the behavior of a single NP in a melt of A homopolymers. The interaction between the polymer segments is varied from $\delta N_{AP} = -50$, corresponding to an attraction between the polymer and the NP, over neutral NPs with $\delta N_{AP} = 0$, to hydrophobic polymers that repel the NPs, $\delta N_{AP} = 50$. We employ a small simulation cell with geometry $3R_{e0} \times 3R_{e0} \times 3R_{e0}$ but use the same spacing of the collocation grid of $\Delta L = 0.05R_{e0}$ as in all other simulations. The width, $R_{PP} - R_{\mathrm{core}} = 0.15R_{e0}$, of the NP surface is resolved by 3 grid points.

Fig. 1(a) shows the average density profiles, $\phi_P(r)$ and $\phi_A(r)$, of NP and polymer beads as a function of the distance from the NP's center. Compared to the continuous NP density plotted directly from Eq. (4), the grid-based $\phi_P(r)$ is closer to the NP center, which originates from the assignment of NP density from the continuous space onto the collocation grid. The inverse compressibility, $\kappa N$, is sufficiently large to expel the polymer beads from the inside of the NP for the repulsive and neutral NPs. However, for the attractive NP, the $\kappa N$-term cannot completely expel the polymer beads due to the lower energy of overlapping NP and A beads. Therefore, we add an additional repulsive hard-sphere potential inside the core of the NPs and reject any trial moves of polymer beads into the NP core. Upon changing the interactions between the NP and the polymer from repulsive to attractive, the homopolymers approach the NP and the interface between the polymer and NP shifts inwards.

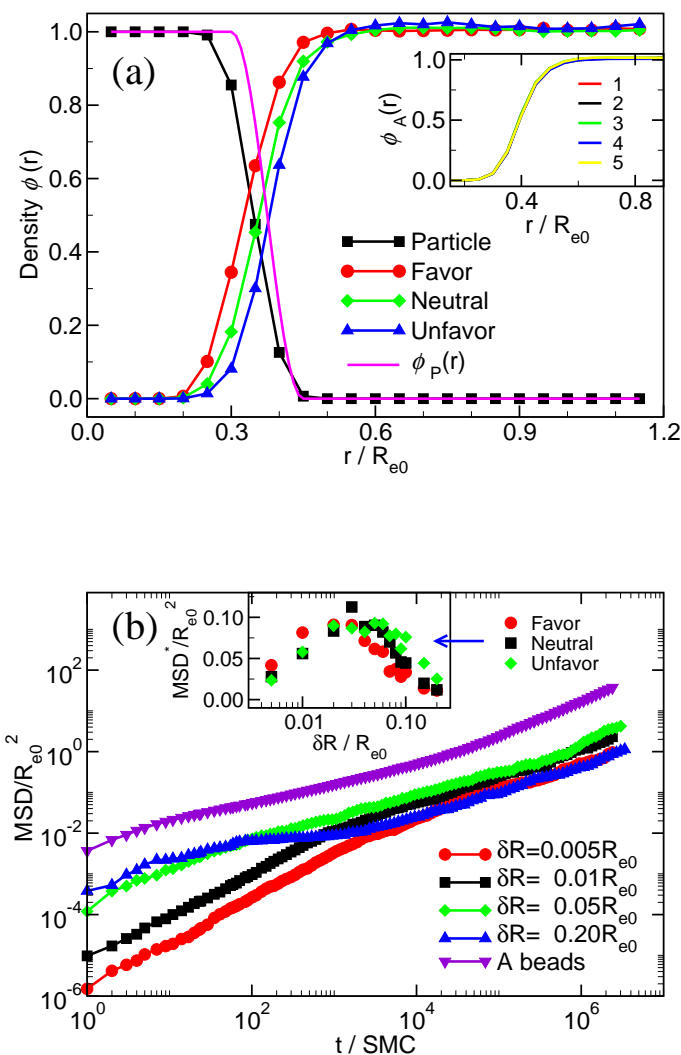**Physical Chemistry Chemical Physics Accepted Manuscript**



FIG. 1: (a) Average densities of NP and polymer beads for various interactions. The inset shows the average density of polymer beads around a repulsive NP fixed at different positions with respect to the collocation grid. (b) Mean-square displacements of repulsive NPs and polymer beads in a homopolymer A matrix. The inset presents the mean-square displacements of NPs at t= 10667SMC as a function of the step length $\delta R$ for various polymer-NP interactions.

In our simulation, the position of NPs and polymer beads can adopt continuous values, whereas the non-bonded interaction is computed via a collocation grid [28]. This collocation grid breaks translational invariance and the density profiles slightly depend on the specific

position of the NP center within a grid cell. To quantify these grid artifacts, we choose 5 random positions of the NP center within one grid cell and calculate the corresponding density profiles for a repulsive NP. The results, shown in the inset of Fig. 1(a), demonstrate that the grid artifacts are vanishingly small for the chosen parameters, i.e., the NP position do not register with the collocation grid and the random off-lattice movement of NPs will not be affected by spurious, grid-based energy barriers.

The monomer positions are updated by Smart Monte Carlo algorithm [33], whereas the configuration of NPs is updated by random, local Monte-Carlo displacements with a maximal trial displacement of $\delta R$ in each Cartesian direction. If $\delta R$ is chosen too small, the NPs do not move far in a MC step. Excessively large values of $\delta R$, in turn, result in a small acceptance ratio of MC moves because of the energy penalty associated with overlaps of NP and surrounding polymer, also giving rise to a slow movement of NPs. To estimate a suitable value of $\delta R$, we study the dynamics of 100 NPs in a system of $3.6 \times 3.6 \times 3.6 R_{e0}^3$.

Fig. 1(b) presents the mean square displacements of NPs in repulsive polymers as a function of $\delta R$, whereas the inset of this panel depicts the mean square displacements at a fixed time $t = 10\,667$ SMC (where at $\delta R = 0.05 R_{e0}$, on average the NPs move in a distance larger than $R_{\text{core}}^2 = 0.09 R_{e0}^2$) as a function of $\delta R$ for various interactions between NPs and polymers. The displacement is maximized by the choice $\delta R^* \approx 0.05 R_{e0}$, and this behavior is rather independent from the NP-polymer interaction. In our simulation we choose a slightly smaller $\delta R = 0.01 R_{e0}$ with the acceptance rate of 0.16.

## III. RESULTS AND DISCUSSION

### A. Influence of condensation ability on the mesoporous thin film

The influence of the two control variables, HCl and water concentration, is captured by varying the strength, $\varepsilon_{PP}$, of attraction between NPs and the affinity, $\delta N_{BP}$ between the NPs and the B block of the amphiphiles. The morphology after passing the drying line is studied by investigating the structure formation from a disordered starting configuration in a slab geometry (see Tab. I). Figure 2(a) shows the morphology evolution of the mesoporous thin films at $\varepsilon_{PP} = 17.0$ and $\delta N_{BP} = 75$. The NPs rapidly segregate from the disordered state in the initial stage, whereas in the later stage the structure gradually coarsens into a disordered

network formed by pores. The statistical properties of the pores, such as the dispersity index (see details in Sec. III C, calculated from 10 independent simulations), however evolves on a protracted time scales of up to $200\,000$ SMC, see Fig. 2(b). Thus in the following, we obtain the statistical properties of the mesoporous thin films for discussion via averaging the configurations between $t = 300\,000$ and $400\,000$ SMC from 10 independent simulations.

One can easily observe in Fig. 2(a) that the pore size obtained at $t = 400\,000$ for $\varepsilon_{PP} = 17.0$ is rather non-uniform (see red arrow). To make a comparison, we show the snapshot of mesoporous thin film obtained from the same $\delta N_{BP} = 75$, but different, lower $\varepsilon_{PP} = 3.0$. Results shown in Fig. 2(a) qualitatively illustrate a uniform pore-size distribution. The time evolution of the dispersity index (see Eq. 16) shown in Fig. 2(b) also confirms that the weak condensation ability gives rise to a rather uniform structure-size distribution.

To quantify this effect, we calculate the normalized size distribution of pores, $P(\sigma)$. The pore area, $\sigma$, is calculated from projected 2D snapshots (see inset of Fig. 2(c)) obtained from the 3D NP density in the slab geometry (see Fig. 2(a)). The results have been averaged over 10 independent simulation runs and for each run 20 snapshots within a time interval between $t = 300\,000$ and $400\,000$ SMC have been analyzed. Fig. 2(c) presents the size distribution of mesopores. This distribution exhibits a maximum at $\sigma_1 = 0.625 R_{e0}^2$ for weak $\varepsilon_{PP} = 3$, with the diameter of the mesopore around $0.89 R_{e0} \simeq 3.53$nm. This is in the same range of the typical Brij58 micelle size ($R_g = 3.2$nm) measured from SAXS [34]. However, the peak of the distribution shifts to $\sigma_2 = 0.75 R_{e0}^2$ at strong $\varepsilon_{PP} = 17$. This result indicates that an increase of the NP condensation ability results in mesoporous structures with larger pores.

We complement this structural information by the calculation of the experimentally accessible, collective structure factor of the NP density,

$$S_{\mathrm{coll}}(\mathbf{q}, t) \sim \left\langle \left| \int d\mathbf{r}\, \phi_P(\mathbf{r}, t) \exp(-i\mathbf{qr}) \right|^2 \right\rangle. \tag{14}$$

and present in Figs. 3(a) and 3(b) the time evolution of the spherical averaged structure factor, $S_{\mathrm{coll}}(q, t) = \langle S_{\mathrm{coll}}(\mathbf{q}, t) \rangle$, for $\varepsilon_{PP} = 3$ and 17. Here the average is performed over 10 independent simulation runs and the different orientations of the wavevector.

The structure factor exhibits a maximum, whose wavevector, $q_{\mathrm{max}}$, is proportional to the inverse distance between the pores illustrated in the snapshots, Figs. 2(a) and 2(b), and whose height increases with time. The increase of the peak height is fast at early stages of
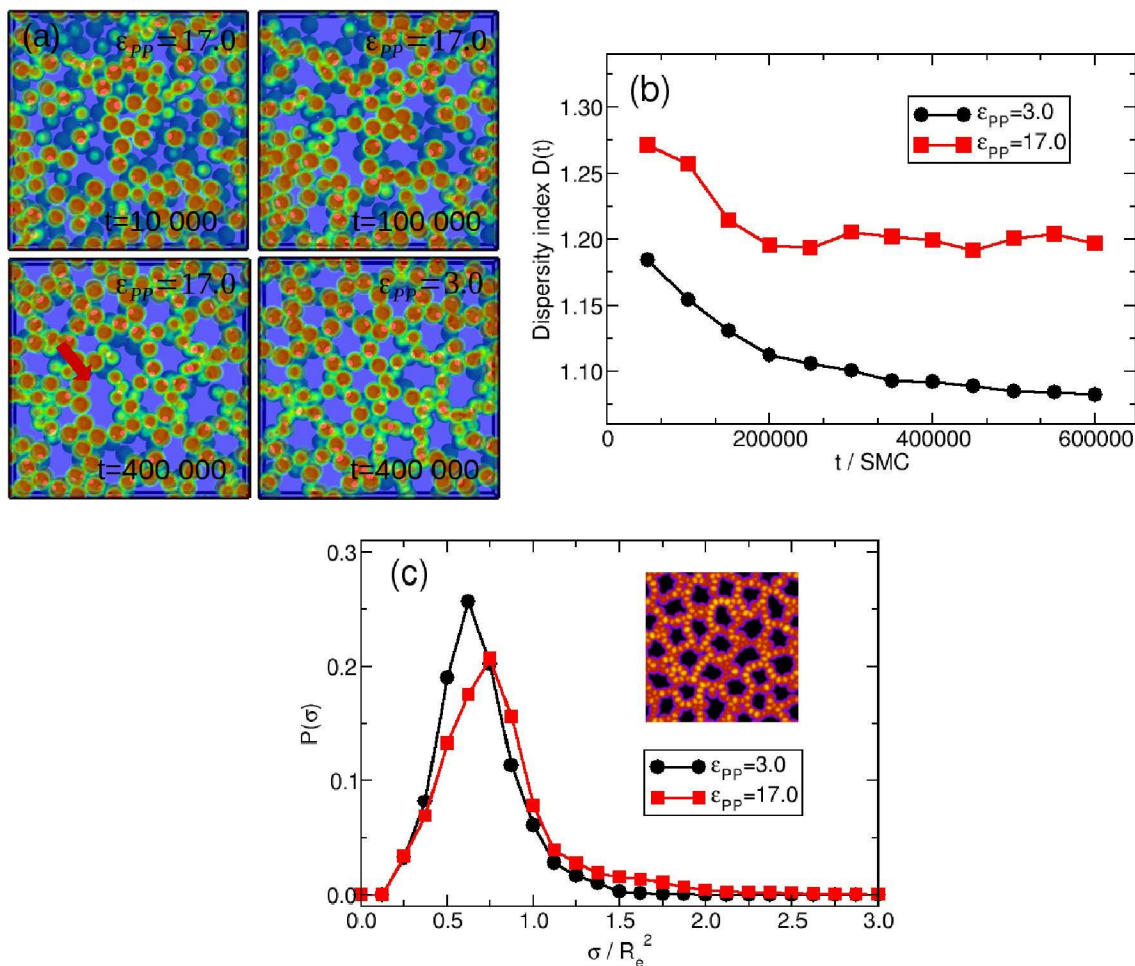
FIG. 2: (a) Typical snapshots of mesoporous structure formed for $\varepsilon_{PP} = 3$ at t=$10\,000, 100\,000, 400\,000$ SMC and $\varepsilon_{PP} = 17$ at t=$400\,000$ SMC. Red spheres represent the NP cores and yellow rings show the interface. Light blue regions are filled by polymers. Red arrows indicate the larger pores. (b) Time evolution of the dispersity index $D(t)$ at $\varepsilon_{PP} = 3$ and 17. (c) Size distributions, $P(\sigma)$, are obtained from 10 independent simulations using a total of 200 configuration snapshots. The inset depicts a 2D snapshot for $\varepsilon_{PP} = 3.0$, from which the distribution of pore areas is calculated.

structure formation, $t < 250\,000$ SMC, and subsequently slows down. For weak $\varepsilon_{PP} = 3$ the structure factor appears to approach a stationary behavior, whereas the peak height continuous to grow and $q_{\max}$ gradually decreases in the course of the simulation for $\varepsilon = 17$. We also note that in the latter case, small-scale structures form at early times, $t = 50\,000$ SMC as indicated by a second peak around $qR_{e0} = 5$.
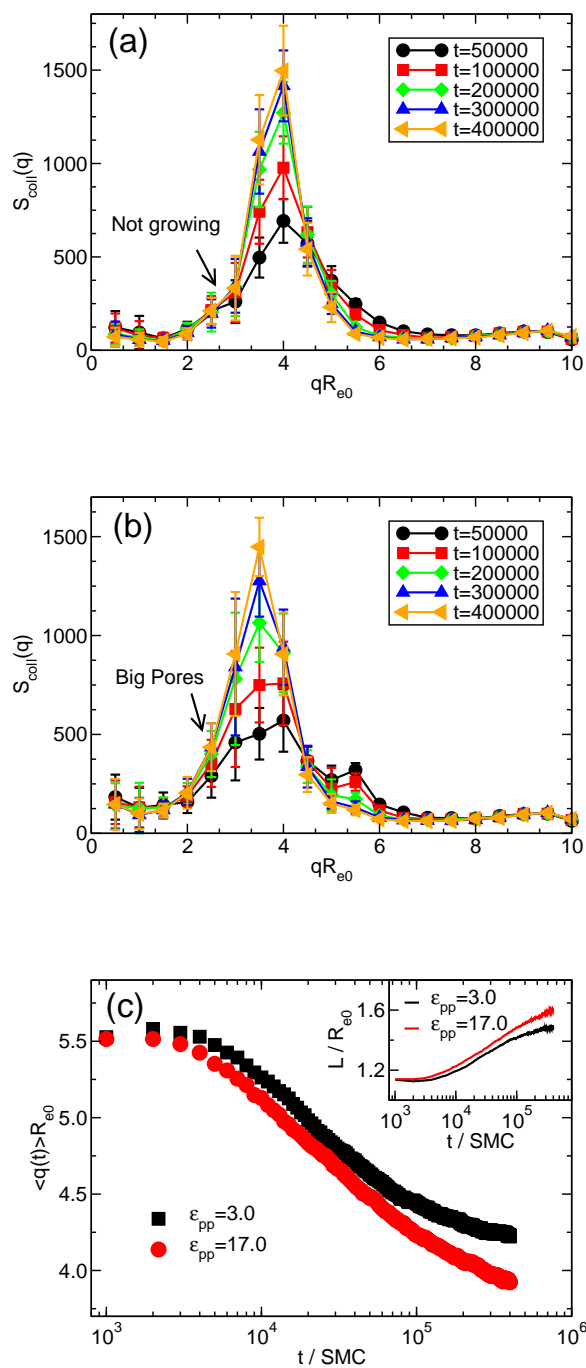
FIG. 3: (a)-(b) Time evolution of the collective structure factors of mesoporous structures formed at time t=50000, 100000, 200000, 300000, and 400000 SMC for $\varepsilon_{PP} = 3$ and 17. The error bar comes from 10 independent simulations. (c) Time evolution of the first moment of the collective structure factor. Inset shows the evolution of the characteristic length.

To quantify the evolution of the characteristic length scale, we consider the first moment of $S_{\mathrm{coll}}(q,t)$

$$\langle q(t) \rangle = \frac{\int \mathrm{d}q \, q S_{\mathrm{coll}}(q,t)}{\int \mathrm{d}q \, S_{\mathrm{coll}}(q,t)} \tag{15}$$

where the integral is extended from $qR_{e0} = 2$ to $9$ around the peak position, c.f. Figs. 3(a) and 3(b). In Fig. 3(c) we present the time evolution of $\langle q(t) \rangle$ for the two condensation abilities, $\varepsilon_{PP} = 3$ and $17$. In both cases, the peak of $S_{\mathrm{coll}}$ initially emerges at $q_{\max} R_{e0} \sim \langle q \rangle R_{e0} \approx 5.6$ and slightly decreases with time. For the weak $\varepsilon_{PP}$, $\langle q(t) \rangle$ appears to cross over to a plateau, $\langle q \rangle R_{e0} \approx 4.2$, whereas $\langle q(t) \rangle$ gradually decreases during the entire simulation for the larger value of $\varepsilon_{PP}$. This is consistent with the larger pore sizes observed in the latter case, c.f. Fig. 2(c).

The snapshots also indicate a possible coarsening mechanism: In the course of (micro)phase separation, the NPs condense into an open network of clusters, whose pores are filled with the structure-directing copolymer. The initial cluster-size distribution is dictated by the spinodal-like phase separation in the NP-copolymer system. For large $\varepsilon_{PP}$, however, there is a strong thermodynamic driving force for additional NP aggregation. This NP aggregation proceeds via a local collapse of some network connections (or pore walls), resulting in a merging of neighboring pores and a concomitant increase of $\langle q \rangle$. This merging of the initially formed pores during the late stages for large $\varepsilon_{PP}$ is supported by the indication of a shoulder in $P(\sigma)$ around $\sigma = 1.75 R_{e0}^2 \approx 2\sigma_{\max}$ and the excess collective scattering around $qR_{e0} \approx 2.5 \approx q_{\max}/\sqrt{2}$. On the scales accessible to our simulation, this coarsening mechanism does not give rise to a self-similar size distribution but rather broadens the size distribution of mesopores and increases their inhomogeneity. We will systematically discuss the variation of pore inhomogeneity as a function of the condensation ability, $\varepsilon_{PP}$, in Sec. III C.

## B. Influence of NP-B block affinity on the pore size distribution

The second, important control variable – the water concentration – is parameterized in our coarse-grained model by the affinity, $\delta N_{BP}$, between the hydrophilic titanium clusters and the B block of the amphiphiles, representing the PEO block. In this section, the condensation ability remains constant, $\varepsilon_{PP} = 3$, and $\delta N_{BP}$ was systematically varied.

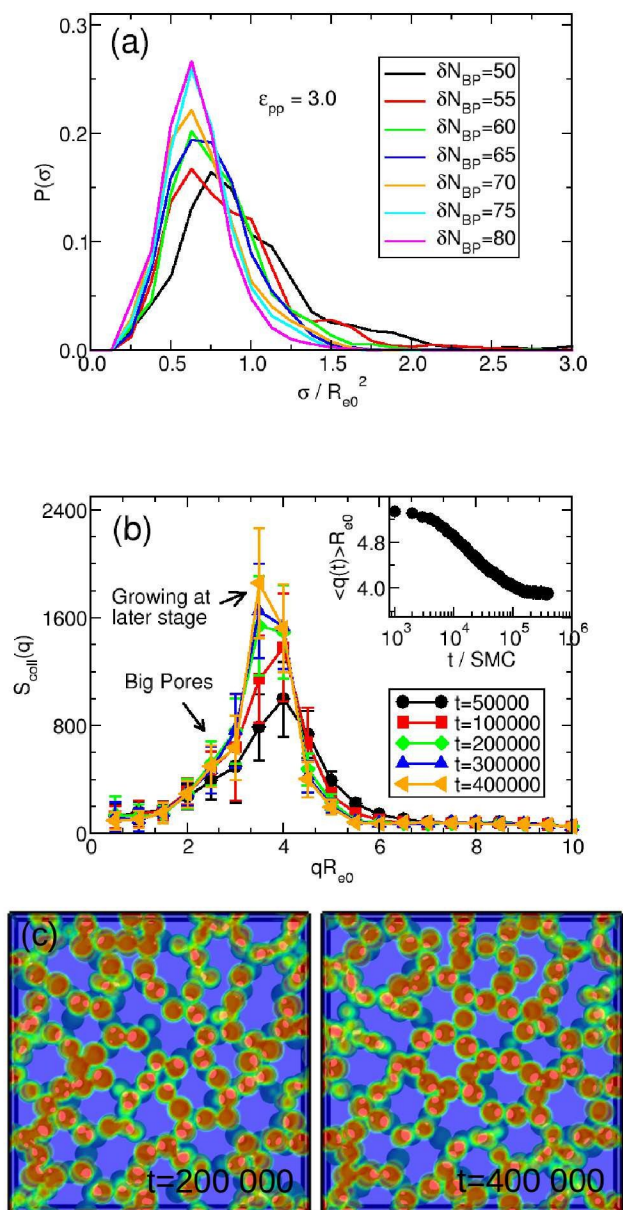Fig. 4(a) presents the variation of the size distribution, $P(\sigma)$, of mesopores as a function

FIG. 4: (a) Size distribution, $P(\sigma)$, of mesopores obtained for different NP-B block affinity at fixed $\varepsilon_{PP} = 3$. Each curve is averaged over 10 independent simulations, using a total of 200 snapshots. (b) Collective structure factor for $\delta N_{BP} = 50$. The main panel presents $S_{\text{coll}}$ at times $t = 50\,000, 100\,000, 200\,000, 400\,000$ SMC using the same statistics for $P(\sigma)$. Inset depicts the time evolution of the structure factor's first moment $\langle q(t) \rangle$. (c) Typical snapshots of mesoporous structure at $t = 200\,000$ and $400\,000$SMC for $\delta N_{BP} = 50$.

of the NP-B block affinity, $\delta N_{BP}$. As $\delta N_{BP}$ increases, the mean pore size decreases and the size distribution becomes narrower, indicating that pore sizes become more homogeneous. Panel (b) depicts the time evolution of the collective structure factor for $\delta N_{BP} = 50$. Qualitatively similar to Fig. 3(a), which uses the same $\varepsilon_{PP}$ but a larger affinity $\delta N_{BP} = 75$, we initially observe a peak in the structure factor at $q_{\max} R_{e0} \approx 4$ that grows and gradually shifts towards smaller wavevectors. The main difference between the two systems is that for the larger affinity, $\delta N_{BP} = 75$ in Fig. 3(a), the system appears to gradually approach a stationary state within the simulation time whereas the height of the collective structure factor $S_{\text{coll}}(q_{\max})$ continuously increases throughout the simulated time window for the weaker affinity, $\delta N_{BP} = 50$ in Fig. 4(b). For the low affinity, $\delta N_{BP} = 50$, however, the peak height of $S_{\text{coll}}$ continues to increase, indicating that the contrast between the NP-rich and polymer-rich regions becomes more pronounced.

The inset of Fig. 4(b) shows the time evolution of $\langle q(t) \rangle$. These values decrease in time, indicating the gradual coarsening of the pore size. At equal times, the characteristic size decreases with the affinity between the PEO-blocks and the titanium-oxo NPs. In both cases of affinity, $\langle q(t) \rangle$ appears to approach a plateau value at the end of the simulated time window. This suggestion is qualitatively supported by the snapshots in Fig. 4(c), depicting local rearrangements of NPs that result in a more compact packing at $t = 4 \times 10^5$ SMC.

In order to quantify the packing of the NPs, in Fig. 5(a), we compare the radial distribution functions, $g(r)$, of the NP centers for different affinities, $\delta N_{BP}$. The direct interaction, $U_{PP}$, between the NPs, Eq. (2), exhibits an attractive minimum at $r_{\min} = 2^{1/6}\sigma_{PP} \approx 0.75 R_{e0}$. This preferred distance is indicated by the vertical line in inset of panel (a). In our simulations, however, we observe that the most probable distance in the NP-copolymer mixture is shifted toward smaller values, and that this decrease is the more pronounced the weaker is the affinity, $\delta N_{BP}$, between the NPs and the hydrophilic block of the copolymers, i.e., there exists an effective, polymer-mediated attraction between the NPs. Its strength can be controlled by $\delta N_{BP}$ which, in turn, is related to the water concentration in the experiment.

This effective, polymer-mediated attraction between NPs is qualitative similar to the depletion interaction in NP-polymer mixtures [35, 36]. Note that the Hamiltonian, $\mathcal{H}_{\text{nb}}^{\text{comp}}$, gives rise to a repulsion between all particle species. In a concentrated polymer solution, the range of the depletion interaction is set by the correlation length of density fluctuations or, equivalently, the width of the interface between the NP and the concentrated solution. This
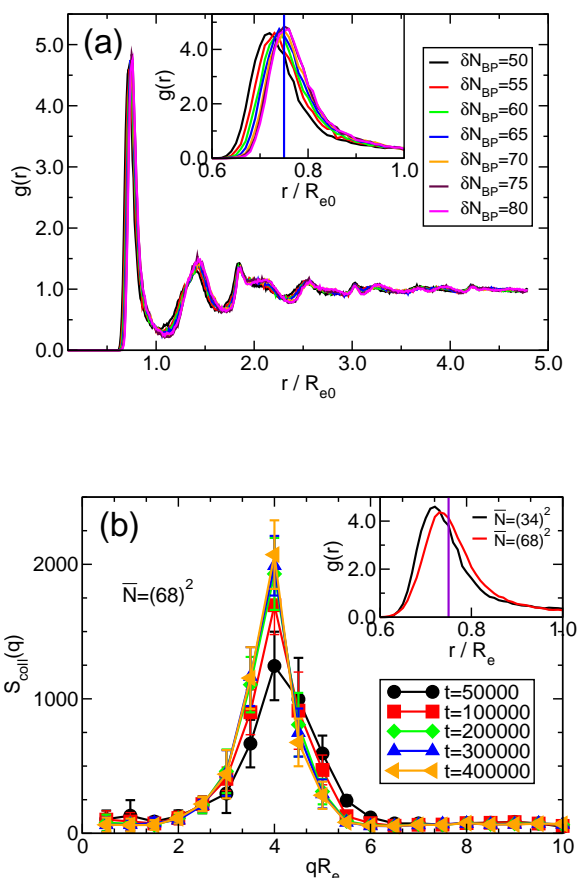
**Physical Chemistry Chemical Physics Accepted Manuscript**

FIG. 5: (a) Radial distribution function, $g(r)$ of NPs at different $\delta N_{BP}$. Inset shows the first peak of $g(r)$, where the vertical blue line labels the distance, $r_{\min} = 2^{1/6}\sigma_{PP} \approx 0.75 R_{e0}$, preferred by the direct interaction, $U_{PP}$, between the NPs. (b) Collective structure factor of mesoporous structure formed with $\sqrt{\mathcal{N}} = 68$ at distinct time $t$. Other parameters are the same as in Fig. 4(b). Inset compares the radial distribution functions for $\sqrt{\mathcal{N}} = 34$ and 68.

length scale decreases with the polymer density as $\xi \sim R_{e0}/\sqrt{z\sqrt{\mathcal{N}}}$ [37] ($z = \upsilon N^2/R_{e0}^3$ is the Fixman parameter with the second-order virial coefficient, $\upsilon = \kappa/\rho_0$), and its effect on the depletion interactions has previously been studied in polymer-colloid systems [38]. In order to validate this rational, we perform additional simulations at a higher copolymer density (increasing $\sqrt{\mathcal{N}}$ from 34 to 68) with modified non-bonded interactions, see Appendix.

Plotting $g(r)$ for the different copolymer densities in the inset of Fig. 5(b), we observe that the preferred NP distance for the higher density is closer to the value, $r_{\min}$, of the direct

interaction, $U_{PP}$, i.e., as expected, the effect of the depletion attraction is much reduced. The time evolution of the collective structure factor for $\sqrt{\mathcal{N}} = 68$ and $\delta N_{BP} = 50$, presented in the main panel of Fig. 5(b), is rather similar to the behavior at low copolymer density but larger affinity, $\sqrt{\mathcal{N}} = 34$ and $\delta N_{BP} = 75$, because $S_{\text{coll}}$ appears to approach a stationary state.

One important difference between the depletion interaction in NP-polymer mixtures that only consider excluded-volume interactions consists in the adsorption of the hydrophilic B block onto the NP. This more complex arrangement of copolymers on the NP surface makes a quantitative comparison to theoretical predictions difficult and, more importantly, allows us to tailor the effective, copolymer-mediated attraction between NPs by the affinity, $\delta N_{BP}$. Increasing $\delta N_{BP}$, the B blocks of the copolymers adsorb onto the NPs and we can reduce the NP attraction, in accord with the data in Fig. 5(a). The increased attraction between NPs at smaller values of $\delta N_{BP}$ thus rationalizes the more compact packing of NPs and the slowing down of coarsening in the late stages presented in Fig. 4.

Both, by increasing $\varepsilon_{PP}$ or decreasing $\delta N_{BP}$, we enhance the attraction between NPs. The local packing structure, however, differs because in the former case, the preferred distance between NPs remains unaltered whereas in the latter case the NPs approach each other. Thus, the difference in local arrangements affects the NP mobility and, potentially, the mechanical properties of the final mesoporous structure.

The simulation result that smaller $\delta N_{BP}$ (high water concentration) generates a broader pore size distribution (low order) could be compared with the experimental observations. In experiments, the freshly deposited films obtained from distinct hydrolysis ratio $h$ were put in a container with the relative humidity (RH) in the range of 10-80% [14]. Results showed that at distinct RH, the intensity of X-ray diffraction peak at high hydrolysis ratio $h$=20 is always smaller than that at $h$=15. This loss of mesoscale ordering for higher $h$ values can be additionally ascribed to a slower evaporation rate, that leads to the formation of ill-defined mesostructures in conditions where the template-inorganic nanobuilding block mesostructure is swollen. In addition, in this swollen structure obtained after longer evaporation times, a significant departure of HCl is expected. Therefore, both issues (dilute medium and enhanced condensation) result in a local order mesostructure with larger interpore distances. This is particularly marked for high RH values.

Other experiments showed that the prolonged treatment of Brij58/TiO$_2$ thin films at

RH> 70% was detrimental to the ordering of mesostructure [16], which can be interpreted in the same vein. These in principle unexpected trends (i.e., decreasing water increases the mesoscopic ordering of mesoporous films) are consistent with our simulation results. It should be noted that further decreasing hydrolysis ratio (water content) to $h \leq 15$, the film morphologies became less ordered [14]. At extremely low RH$\leq$ 15% and small $h \leq 5$, no organized morphology emerges. These results are summarized as an empirical conclusion: adding water improves the order of mesoporous thin films [14]. The reason why our model cannot reproduce this phenomenon can be explained as follows. In the extremely low water content, the strong chelation interaction (the magnitude is similar to the bonded interaction between monomers) between the titanium precursors and PEO templates significantly changes the configuration of the PEO chain [17], forming an effective "hybrid molecule". In this sense, our soft coarse-grained modeling of the Brij58 and titanium precursors as independent entities is not sufficient to capture the chemical details and also the dynamics in real experiments. Alternative simulation models, accounting for the strong chelations between the titanium precursors and PEO templates, are required for explaining the effects of water at extremely low water content.

### C. Dispersity of mesopores

From above discussion, we found that both the condensation ability $\varepsilon_{PP}$ and the NP-B block affinity $\delta N_{BP}$ can influence the size distribution of formed mesopores (see the $P(\sigma)$ in Fig. 2(c) and Fig. 4(a)). It would be interesting to explore this influence via systematically varying the parameters of $\varepsilon_{PP}$ and $\delta N_{BP}$. Before we proceed to next step, it would make the analysis easier by defining an "order parameter", which could characterize the variation of size distribution of mesopores. This can be done by calculating the dispersity index of the mesopore area, defined by

$$D = \frac{S_w}{S_n} \tag{16}$$

where $S_w = \Sigma_i n_i \sigma_i^2 / \Sigma_i n_i \sigma_i$ is the weight average pore area and $S_n = \Sigma_i n_i \sigma_i / \Sigma_i n_i$ is the number average pore area. Here $n_i$ is the number of mesopores with area $\sigma_i$ obtained from 10 independent simulations, in each simulation 20 configurations between $t = 300\,000$ and $400\,000$ SMC are selected for the calculation. This index is similar to the one characterizing the dispersity of molecular weight of polymers, here it is the "order parameter" for labelling
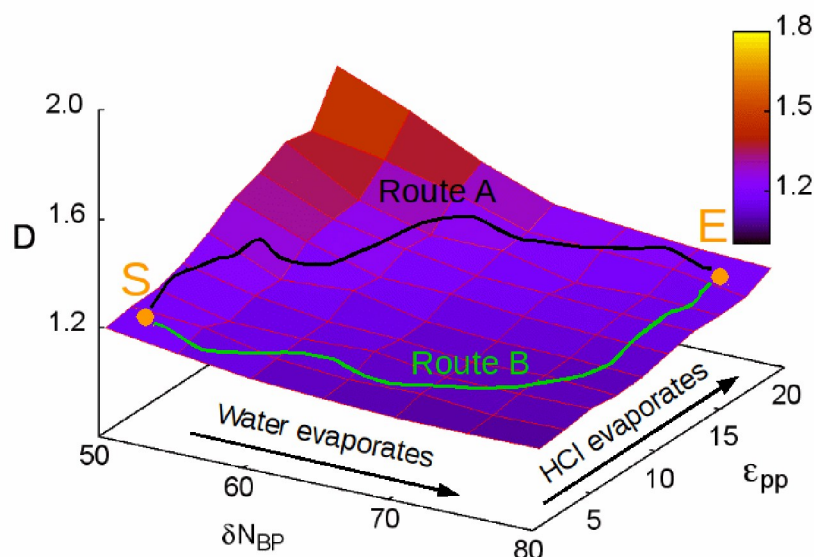
FIG. 6: Variation of the dispersity index $D$ as a function of the NP-B block affinity $\delta N_{BP}$, and the NP-NP condensation ability $\varepsilon_{PP}$.

the homogeneity of the formed mesopores in terms of area. The smaller the dispersity index $D$, the more uniform the formed mesopores. As an example, for the two cases shown in Fig. 2, the calculated dispersity index $D$ is 1.09 for $\varepsilon_{PP} = 3.0$ and 1.17 for $\varepsilon_{PP} = 17.0$. Obviously it could also be employed as an indicator for the order of the mesoporous thin films. The small $D$ of homogeneous pore distribution indicates a high order of the formed films, and vice versa.

Figure 6 shows the variation of dispersity index as a function of the condensation ability $\varepsilon_{PP}$ and the NP-B block affinity $\delta N_{BP}$. It is clearly shown that at weak $\varepsilon_{PP}$ and high $\delta N_{BP}$, the system favors the homogeneous size distribution, while at strong $\varepsilon_{PP}$ and low $\delta N_{BP}$, the pore size distribution shows non-uniform behaviour. The size difference can also be seen in experimental mesoporous thin films. Figure 7 shows the 2D-SAXS pattern for two typical Brij58 templated TiO2 samples. Both samples were prepared with the same proportions, according to the literature [14]. However, the drying after film synthesis proceed differently and, as consequence, the obtained degree of order is different. For the sample (a) the pattern of an Im3m cubic array of mesopores is observed. For such sample, the [110] interplanar distance (i.e. the average distance between the pores in the film's surface, derived from SAXS and TEM studies) is $d_{110} = 6.32$ nm. For sample (b), the obtained ellipse indicates a lower degree of order in the mesoporous structure with locally ordered mesopores. For such

sample, $d_{110} = 6.45$ nm. The larger interpore distance obtained for the disordered structure is consistent with our simulation results shown in Fig.2(c).

As discussed previously, the condensation ability between NPs in real experiments is mainly controlled by the acidity in the solution, while the NP-B block affinity depends on the volume fraction of water. For the freshly deposited films, both the $\varepsilon_{PP}$ and $\delta N_{BP}$ are small due to the existence of residual water and acid. In the course of the co-assembly process, water evaporates until a dynamical equilibrium with the humid atmosphere (controlled by RH from experiments) is achieved, leading to an increase of $\delta N_{BP}$. However, the exchange of water between the film and the atmosphere drives the continuous evaporation of HCl, giving rise to an increase of $\varepsilon_{PP}$. In most cases, water and acid evaporates simultaneously, but with different evaporation rates [14]. This gives rise to different variation rates of $\varepsilon_{PP}$ and $\delta N_{BP}$, thereby generating two possible routes (plotted as route A and route B in Fig.6) when the system evolves from the initial state ($S$) towards final state ($E$). For the route A, the $\varepsilon_{PP}$ increases rapidly compared to the $\delta N_{BP}$, thus the system enters the high dispersity region first, then approaches the end point. During this process, if there exists some free-energy barriers between the high dispersity region and the end point, the system might be trapped in the high-dispersity region with non-uniformed pore-size distribution. While for the route B, $\delta N_{BP}$ increases quickly compared to $\varepsilon_{PP}$, and the system first enters into lower-dispersity area. In this area, the system normally stays in a favorable metastable state, where further evaporation of HCl (increase of $\varepsilon_{PP}$) can not easily change the morphologies. Thus, with high probability, the formed mesopores show a uniform size distribution. These arguments imply that different evaporation rates between water and acid might drive the system into metastable states with uniform or non-uniform pores, respectively. Although Fig. 6 does not provide a real kinetic route, the above arguments still provide some intuitive understandings about the influence of the distinct evaporation rates of co-solvents on the pore-size distribution of mesostructured thin films.

### D. Post processing of mesoporous thin films

In experiments, the obtained mesoporous thin films sometimes show non-uniform pore size distributions due to the complex preparation history. In this case, a post-processing treatment is normally employed to process the sample towards high ordered mesoporous
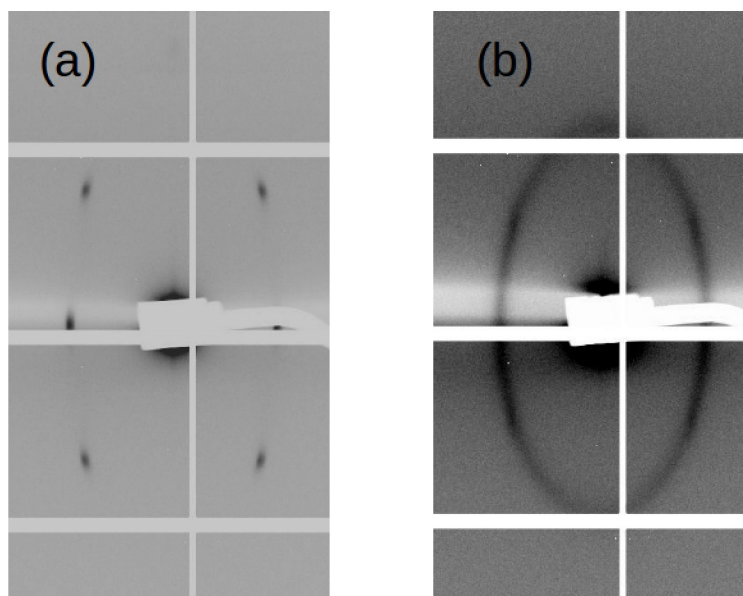
FIG. 7: 2D SAXS patterns for the mesoporous structure formed with Titanium precursors using Brij58 as template. (a) Ordered structure with $d_{110} = 6.32$nm. (b) Disordered structure with $d_{110} = 6.45$nm.

structure [39, 40]. For titanium mesoporous thin films, the post-treatment procedure normally indicates the aging of freshly deposited thin films under intermediate external humidity (RH between 20 and 70%) [40]. Recently, new ellipsometry-based experiments were employed to monitor the evolution of refractive index of the freshly deposited titanium thin films to identify the drying-swelling behaviour [2]. At short times, when the RH increased from 25% and 65%, the refractive index of the film decreased dramatically, indicating the existence of liquid water (with very low refractive index) in the film, while at longer times, the refractive index increased as RH increases, implying the fully condensation of the film. Thus the post-treatment at certain RH is only available for freshly deposited films where the water could swell the films before the titanium clusters condensed together. The key point of the post-processing is to rearrange the titanium clusters towards high ordered mesostructures.

To confirm the behaviour of "post-processing towards high order", in our simulation we could make the rearrangement of NPs possible by weakening the strong condensation ability $\varepsilon_{PP}$. Here we choose the high dispersity index configurations at $\varepsilon_{PP} = 17.0$ (see typical snapshot at $t = 400\,000$ SMC in Fig. 2(a)) as initial states and perform the simulations at weak $\varepsilon_{PP} = 3.0$. This process mimics the post-processing of the non-uniformed sample at high RH. Figure 8(a) shows the size distribution before and after the post processing.
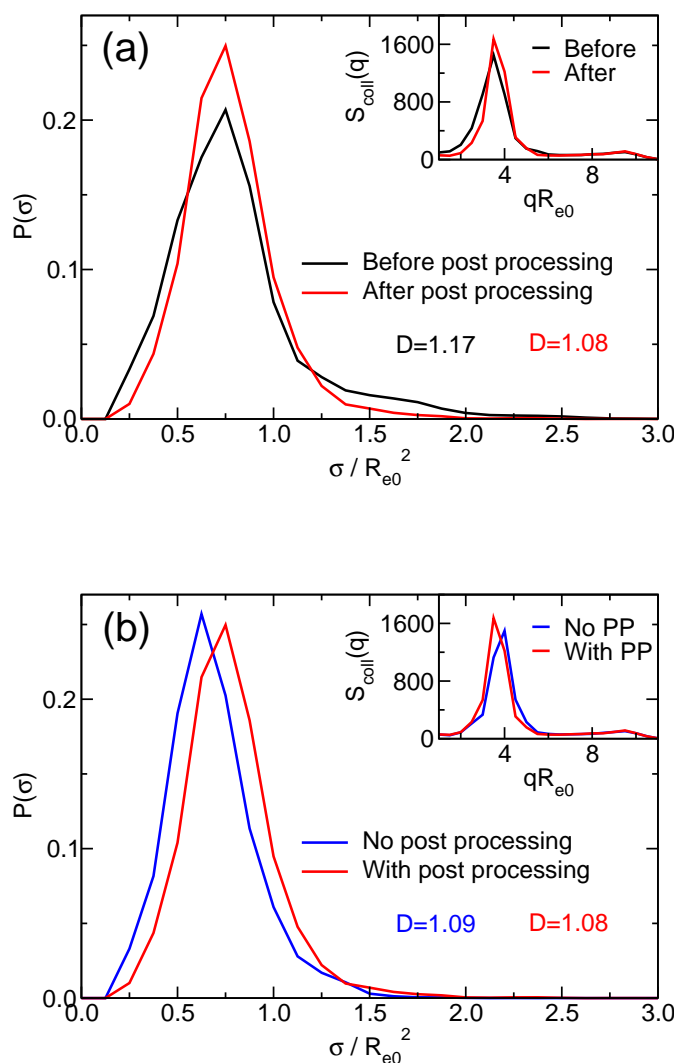
FIG. 8: (a) Size distribution of mesopores before and after the post processing treatment. (b) Comparison of the pore size distribution initially evolves from $\varepsilon_{PP} = 3.0$ and after post processing at $\varepsilon_{PP} = 3.0$. Both insets show the comparison of the corresponding collective structure factors (error bars are omitted for clear display).

It is clearly shown that the peak of pore size distribution becomes narrower, and the long tail region of $P(\sigma)$ (with $\sigma > 1.5R_e^2$) disappears after the post-processing treatment. The dispersity index $D$ indeed decreases from 1.17 to 1.08 after post processing, confirming the phenomena of "post-processing towards high order". The comparison between the structure factors at t=400 000SMC (see inset of Fig. 8(a)) also shows a narrower peak after post

processing, indicating the more uniform mesostructured thin films.

Interestingly, we find that the dispersity index after post processing $D = 1.08$ is nearly equal to the value of $D = 1.09$ obtained from the mesoporous structure directly formed at weak condensation ability $\varepsilon_{PP} = 3.0$. We compare the size distribution and the collective structure factor of these two different cases, see Fig. 8(b). The shape of the two size distribution peaks are nearly the same, with only a small shift of the maximum. This implies that one can use the post processing treatment to obtain the mesostructured thin films with uniform but slightly larger pores, which provides an alternative way to tune the pore size of the uniform mesostructured thin films.

### E. Discussion

In previous sections, we have shown that the soft coarse-grained models of block copolymers and nanoparticles (NPs) can be employed to simulate and study the co-assembly of the surfactant Brij58 and titanium subunit clusters towards ordered mesostructured $TiO_2$ thin films. The complex roles of the water and HCl during the co-assembly process has implicitly been incorporated into the interactions of NP-B block affinity $\delta N_{BP}$ and the NP-NP condensation ability $\varepsilon_{PP}$. The obtained results show how the two parameters independently influence the pore size distribution, and also the dispersity index of the mesoporous thin films. These findings successfully confirm the distinct roles of water and HCl on the final mesostructured thin films.

Although the simulation results are in good agreements with experiments, there are still some important aspects that cannot be captured by our models. For example, the lack of explicitly consideration of water makes it impossible to consider the local swelling induced by water, such as water from air (high RH). As measured in experiments [14], the film thickness at RH=70% is nearly twice as that at RH≤ 20%. This excess amount of water is mainly filled in the hydrophilic region constructed by titanium clusters and PEO chains, resulting in the increase of the effective volume fraction of hydrophilic species during the co-assembly process. This gives rise to the transition of the system towards highly curved phase [40]. Another point is that the effective H-bonds or intermolecular interactions between water and HCl might influence the distinct evaporation rates of HCl and water. Also, as pointed out in Sec. III B, at very low water content, the strong chelation interaction (the magnitude

is at the level of covalent bond) between titanium cores and the PEO chains will change the structure of the amphiphilic surfactants, which makes our soft coarse-grained models of surfactants unreliable in this extremely low water situation.

However, the outlined simulation procedure still holds advantages. For example, our simulation procedure enables the investigation of the influence of one parameter (such as $\varepsilon_{PP}$ and $\delta N_{BP}$) on the final mesoporous structure while keeping all the other parameters constant, which is not easy to be done in experiments due to the simultaneous variation of all the contributions. This is useful for identifying the different mechanisms, such as entropic attractions, on the final mesostructured thin films. Also the simulations can account for the kinetics of the co-assembly at specific parameters via monitoring the time evolution of the structure factors, as discussed in the previous sections.

Previous simulations have studied the synthesis and formation of ordered mesoporous silica materials by directly considering the sol-gel process of silicon precursors [41]. A lattice model, which ignores the microscopic silica condensation kinetics and monomer mass transport, was employed to simulate the silica polymerization during sol-gel process [42]. The distribution of the fraction of silicon atoms connected to $n$ bridging oxygen atoms has been calculated from simulation, in good agreement with experimental NMR results [43]. Based on the same model, a two step simulation procedure has been chosen to study the formation of mesoporous silica materials [44]: in the first step, the silicon precursors and surfactant spontaneously form into lamellar or hexagonal ordered structures, while in the second step, the silica condensation was initiated to obtain the high ordered hexagonal arrays. This two-step procedure is available for silica systems due to the slow reactivity of silica precursors. However, for the titanium precursors, the high reactivity indicates that the condensation already occurs during the co-assembly process [45], and makes it difficult to separate the self-assembly of surfactants and the condensation of titanium clusters.

It is also worthy to compare our simulations with the self-assembly of block copolymer and nanoparticle (BCP-NP) composites. Most of the driving force of BCP-NP composites comes from the requirements of enhanced mechanical, optical, electrical, and photovoltaic properties of the formed nanomaterials [46–50]. The prepared nanoparticles with controlled size (normally comparable to the polymer coil size), shape, and surface properties were embedded into selected domain of phase-separated block copolymers via melt mixing or solution casting, generating ordered block polymer-nanoparticles composites with desired properties.

**Physical Chemistry Chemical Physics Accepted Manuscript**

In most of the cases, the interactions of polymer-NP and NP-NP stay nearly constant during the co-assembly process. Based on this feature, many theories [51–55] and simulations [56, 57] were employed to study the phase behaviors of these composites. Although the investigated system in our simulations (block copolymers and titanium-oxo clusters) looks similar to the widely investigated BCP-NP composites, the addressed issues are very different. During the formation of mesostructured $TiO_2$ thin films, the co-solvents such as water and HCl play vital roles during the co-assemble process via influencing the BCP-NP and NP-NP interactions. Our modeling process simplifies the simulations by incorporating the effects of water and HCl independently into distinct interactions to study its role on the formation of final mesostructure. The outlined procedure paves the way for investigating the co-assembly process of transition metal precursors and amphiphilic surfactants via coarse-grained models, only with the need of careful handling of the effects of versatile water and condensation inhibitors HCl during the formation process. We anticipate that this approach can also be very useful to understand the mechanisms of formation of films or aerosols obtained via inhibitors such as acetylacetone [58] and novel low-valence mesoporous oxides (i.e., NiO, CoO, $Al_2O_3$) that use the self-assembly of pre-formed inorganic nanobuilding blocks with block-copolymer SDA [59].

## IV.   CONCLUSION

In summary, we employ the soft coarse-grained model of amphiphilic surfactant Brij58 and spherical particles of titanium subunit clusters to study the role of HCl and water on the formation of mesostructured $TiO_2$ thin films. The formation kinetics of mesoporous thin films are systematically studied and compared at different condensation ability $\varepsilon_{PP}$ and the NP-B block affinity $\delta N_{BP}$. Results show that the effective attraction between NPs could be enhanced both by increasing $\varepsilon_{PP}$ or decreasing $\delta N_{BP}$. The local packing structure, however, differs because in the former case, the preferred distance between NPs remains unaltered whereas in the latter case the NPs approach each other. This gives rise to the various mesoporous properties. The variation of dispersity index on the $\delta N_{BP}$-$\varepsilon_{PP}$ plane indicates that the slow evaporation of HCl might drive the film into uniform mesoporous thin films while the fast evaporation pushes the film into non-uniformed phase. These results indicate that even the mass proportion of the surfactants Brij58 and titanium precursors

**Physical Chemistry Chemical Physics Accepted Manuscript**

is the same in the initial solution, the final mesoporous structures could be diverse, which was confirmed by the controlled experiments. We also confirm the "post-processing towards order" via making the rearrangement of NPs available by weakening the condensation ability $\varepsilon_{PP}$. This in-depth understanding opens the path for a rational design of a variety of thin films or colloidal mesoporous materials with multiple applications.

## Acknowledgments

## A.   Appendix: Concentration induced depletion effects in grid based simulation

Within the grid implementation of our coarse-grained model, the increase of polymer density $\sqrt{\mathcal{N}} = \rho_0 R_{e0}^3 N^{-1}$ does not change the interface width. We can make a simple test of one single NP immersed in a A homopolymer matrix. In this situation, the non-bonded interactions simplify as:

$$\frac{\mathcal{H}_{\mathrm{nb}}^{\mathrm{comp}}}{k_B T} = \sqrt{\mathcal{N}} \int \frac{\mathrm{d}\mathbf{r}}{R_{e0}^3} \frac{\kappa N}{2} [\phi_A(\mathbf{r}) + \phi_P(\mathbf{r}) - 1]^2 \tag{17}$$

The interactions between A homopolymer and NP are set to be neutral, $\delta N_{AP} = 0$, while $\kappa N$ is set to be 80. The A monomer density near the NP shown in the inset of Fig. 10 clearly demonstrates that the interface does not change as $\sqrt{\mathcal{N}}$ (polymer concentration in our simulation) increases from 34 to 68. To account for this phenomenon, we write the normalized density $\phi_A(\mathbf{r}) = \rho_0^{-1} \sum_{i,s=1}^{n,N} \delta(\mathbf{r} - \mathbf{r}_{i,s})$ on grid-based cell $c$ as

$$\phi_A(c|\{\mathbf{r}\}) = \frac{1}{\rho_0 \Delta L^3} \sum_{i,s=1}^{n,N} \Pi(c, \mathbf{r}_{i,s}) \tag{18}$$

Here $\Pi(c, \mathbf{r})$ is the assignment function which obeys [29]

$$\sum_c \Pi(c, \mathbf{r}) = 1 \;\; \forall \mathbf{r} \quad \text{and} \quad \int \mathrm{d}\mathbf{r} \Pi(c, \mathbf{r}) = \Delta L^3 \;\; \forall c \tag{19}$$
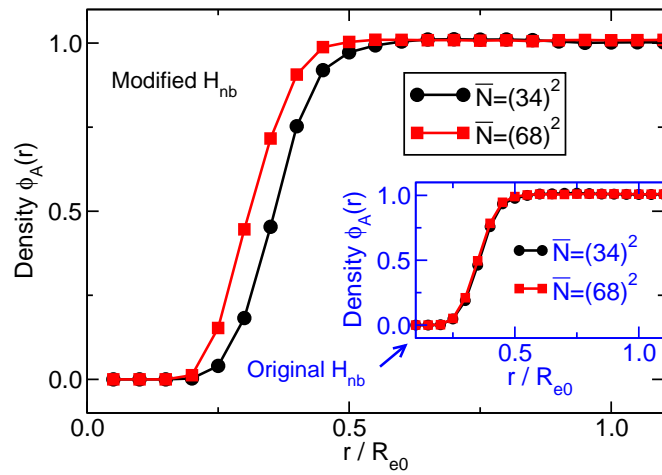
FIG. 9: Average density of homopolymer A near one neutral NP at $\sqrt{\overline{\mathcal{N}}} = 34$ and 68.

The integral of squared A density can be rewritten as

$$
\begin{aligned}
\frac{\kappa N \sqrt{\overline{\mathcal{N}}}}{2 R_{e0}^3} &\int \mathrm{d}\mathbf{r} [\phi_A(\mathbf{r})]^2 = \\
\frac{\kappa N \sqrt{\overline{\mathcal{N}}}}{2 R_{e0}^3} &\sum_c \Delta L^3 \frac{1}{\rho_0^2 \Delta L^3 \Delta L^3} \sum_{i,s,j,k} \Pi(c, \mathbf{r}_{i,s}) \Pi(c, \mathbf{r}_{j,k}) \\
&= \frac{1}{N^2} \sum_{i,s,j,k} \upsilon(\mathbf{r}_{i,s}, \mathbf{r}_{j,k})
\end{aligned}
\tag{20}
$$

Here the pair wise interaction between two monomers at $\mathbf{r}_{i,s}$ and $\mathbf{r}_{j,k}$ is

$$
\upsilon(\mathbf{r}_{i,s}, \mathbf{r}_{j,k}) = \frac{1}{\sqrt{\overline{\mathcal{N}}}} \frac{\kappa N}{2} \frac{R_{e0}^3}{\Delta L^3} \sum_c \Pi(c, \mathbf{r}_{i,s}) \Pi(c, \mathbf{r}_{j,k})
\tag{21}
$$

which decreases as the monomer density $\sqrt{\overline{\mathcal{N}}}$ increases from 34 to 68. This results in the invariant of A density square term in Eq. 20, and thus the A density profile near nanoparticle (see inset of Fig. 10).

To reveal the depletion effects induced by the increase of monomer density [37], we choose $\phi'_A(\mathbf{r}) = \alpha \phi_A(\mathbf{r})$ to make the pair wise interaction $\upsilon(\mathbf{r}_{i,s}, \mathbf{r}_{j,k})$ invariant as monomer concentration $\sqrt{\overline{\mathcal{N}}}$ increases from 34 to 68. Here $\alpha = \sqrt{\sqrt{\overline{\mathcal{N}}}_{68}/\sqrt{\overline{\mathcal{N}}}_{34}} = \sqrt{2}$ is the ratio of monomer concentration at different $\sqrt{\overline{\mathcal{N}}}$. Inset $\phi'_A(\mathbf{r})$ into Eq.17, we obtain

$$
\frac{\mathcal{H}_{\mathrm{nb}}^{\mathrm{comp}\prime}}{k_B T} = \sqrt{\overline{\mathcal{N}}} \int \frac{\mathrm{d}\mathbf{r}}{R_{e0}^3} \frac{\kappa N}{2} [\phi'_A(\mathbf{r}) + \phi_P(\mathbf{r}) - 1]^2
\tag{22}
$$

30

However, as $\phi_P(\mathbf{r})$ does not change during the variation of $\sqrt{\mathcal{N}}$, the integral of $\int \mathrm{d}\mathbf{r}\phi'_A(\mathbf{r})\phi_P(\mathbf{r})$ depends unphysically on $\alpha$. To eliminate this effect, we choose $\phi'_P(\mathbf{r}) = \alpha^{-1}\phi_P(\mathbf{r})$ and inset it into Eq.22. Eventually we obtain the modified nonbonded interaction term

$$\frac{\mathcal{H}_{\mathrm{nb}}^{\mathrm{comp}\prime}}{k_B T} = \sqrt{\mathcal{N}}_{34} \int \frac{\mathrm{d}\mathbf{r}}{R_{e0}^3} \frac{\kappa N}{2}[\alpha^2\phi_A(\mathbf{r}) + \phi_P(\mathbf{r}) - 1]^2 \tag{23}$$

here the last term was set to 1 by adding some constants. Physically, the $\alpha^2\phi_A(\mathbf{r}) = \rho_0\phi_A(\mathbf{r})/\rho_0(34)$ indicates the unnormalized A monomer density. With this modified nonbonded interaction, we observe a clear narrowed monomer interface near one neutral nanoparticle, see Fig. 10. We can estimate the narrowing percentage of the interface from Fig. 10 by $(7-5)/7 \simeq 0.286$, here 7 and 5 are the grids occupied by the interface at $\sqrt{\mathcal{N}} = 34$ and 68. From the theoretical prediction [37], the depletion layer scales with the monomer concentration by $\xi \sim R_{e0}/\sqrt{z\sqrt{\mathcal{N}}}$. We can also estimate the narrowing percentage of $(R_{e0}/\sqrt{34} - R_{e0}/\sqrt{68})/(R_{e0}/\sqrt{34}) \simeq 0.293$. The consistency between simulation result and the theoretical prediction indicates that the modified interaction, Eq. (23), can account well for the concentration induced depletion effects in grid-based implementation of our coarse-grained simulations. Although the above discussion is about the non-preferential nanoparticle immersed in homopolymer A matrix, similar narrowing interface is also observed for the case of attractive nanoparticle.

Based on the above discussion, we can rewrite the nonbonded interactions for the AB block copolymers and nanoparticles as:

$$\begin{aligned}
\frac{\mathcal{H}'_{\mathrm{nb}}}{k_B T} =& \sqrt{\mathcal{N}}_{34} \int \frac{\mathrm{d}\mathbf{r}}{R_{e0}^3}\{\frac{\kappa N}{2}[\alpha^2\phi_A(\mathbf{r}) + \alpha^2\phi_B(\mathbf{r}) + \phi_P(\mathbf{r}) \\
& - 1]^2 - \frac{\delta N_{AP}}{4}[\alpha^2\phi_A(\mathbf{r}) - \phi_P(\mathbf{r})]^2 + \frac{\delta N_{BP}}{4}[ \\
& \alpha^2\phi_B(\mathbf{r}) - \phi_P(\mathbf{r})]^2\} - \sqrt{\mathcal{N}} \int \frac{\mathrm{d}\mathbf{r}}{R_{e0}^3} \frac{\chi N}{4}[\phi_A(\mathbf{r}) \\
& - \phi_B(\mathbf{r})]^2
\end{aligned} \tag{24}$$

Here the last term which characterizes the phase separation between A and B blocks does not change, to make sure that the AB diblock copolymers do not enter other phases by increasing the monomer density. This modified nonbonded interactions could account for the concentration induced depletion effects between nanoparticles in B domains, and simultaneously ensure that the variation of pore size distribution does not originate from the phase transition of AB diblock copolymers. With this modified nonbonded interactions, we per-

formed the controlled simulations at $\sqrt{\mathcal{N}} = 68$ and calculate the evolution of the collective structure factors and the corresponding radial distribution function, as shown in Fig. 5(b).

[1] S. W. Boettcher, J. Fan, C.-K. Tsung, Q. Shi, and G. D. Stucky, Acc. Chem. Res. **40**, 784 (2007).

[2] G. J. de A. A. Soler-Illia, P. C. Angelomé, M. C. Fuertes, D. Grosso, and C. Boissiere, Nanoscale **4**, 2549 (2012).

[3] R. Zhang, D. Shen, M. Xu, D. Feng, W. Li, G. Zheng, A. A. E. Renchao Che, and D. Zhao, Adv. Energy Mater. **4**, 1301725 (2014).

[4] W. Li, J. Liu, and D. Zhao, Nat. Rev. Mater. **1**, 16023 (2016).

[5] H. suk Yun, K. Miyazawa, H. Zhou, I. Honma, and M. Kuwabara, Adv. Mater. **13**, 1377 (2001).

[6] P. C. A. Alberius, K. L. Frindell, R. C. Hayward, E. J. Kramer, G. D. Stucky, and B. F. Chmelka, Chem. Mater. **14**, 3284 (2002).

[7] G. J. de A. A. Soler-Illia and P. Innocenzi, Chem. Eur. J. **12**, 4478 (2006).

[8] J. H. Pan, X. S. Zhao, and W. I. Lee, Chem. Eng. J. **170**, 363 (2011).

[9] R. Zhang, A. A. Elzatahry, S. S. Al-Deyab, and D. Zhao, Nano Today **7**, 344 (2012).

[10] W. Li, Z. Wu, J. Wang, A. A. Elzatahry, and D. Zhao, Chem. Mater. **26**, 287 (2014).

[11] Y. Lu, R. Ganguli, C. A. Drewien, M. T. Anderson, C. J. Brinker, W. Gong, Y. Guo, H. Soyez, B. Dunn, M. H. Huang, and J. I. Zink, Nature **389**, 364 (1997).

[12] C. J. Brinker, Y. Lu, A. Sellinger, and H. Fan, Adv. Mater. **11**, 579 (1999).

[13] D. Grosso, G. J. de A. A. Soler-Illia, F. Babonneau, C. Sanchez, P.-A. Albouy, A. Brunet-Bruneau, and A. R. Balkenende, Adv. Mater. **13**, 1085 (2001).

[14] E. L. Crepaldi, G. J. de A. A. Soler-Illia, D. Grosso, F. Cagnol, F. Ribot, and C. Sanchez, J. Am. Chem. Soc. **125**, 9770 (2003).

[15] D. Grosso, C. Boissière, B. Smarsly, T. Brezesinski, N. Pinna, P. A. Albouy, H. Amenitsch, M. Antonietti, and C. Sanchez, Nat. Mater. **3**, 787 (2004).

[16] M. J. Henderson, A. Gibaud, J. F. Bardeau, and J. W. White, J. Mater. Chem. **16**, 2478 (2006).

[17] G. J. de A. A. Soler-Illia, E. Scolan, A. Louis, P.-A. Albouy, and C. Sanchez, New. J. Chem. **25**, 156 (2001).

[18] J. Livage, M. Henry, and C. Sanchez, Prog. Solid. State Chem. **18**, 259 (1988).

[19] E. G. Solveyra, M. C. Fuertes, G. J. A. A. Soler-Illia, and P. C. Angelomé, J. Phys. Chem. C **121**, 3623 (2017).

[20] D. M. Antonelli and J. Y. Ying, Angew. Chem. Int. Ed. **34**, 2014 (1995).

[21] J. Zhang, Y. Deng, D. Gu, S. Wang, L. She, R. Che, Z.-S. Wang, B. Tu, S. Xie, and D. Zhao, Adv. Energy Mater. **1**, 241 (2011).

[22] A. Vioux, Chem. Mater. **9**, 2292 (1997).

[23] P. Yang, D. Zhao, D. I. Margolese, B. F. Chmelka, and G. D. Stucky, Nature **396**, 152 (1998).

[24] J. M. Szeifert, J. M. Feckl, D. Fattakhova-Rohlfing, Y. Liu, V. Kalousek, J. Rathousky, and T. Bein, J. Am. Chem. Soc. **132**, 12605 (2010).

[25] B. Tian, H. Yang, X. Liu, S. Xie, C. Yu, J. Fan, B. Tu, and D. Zhao, Chem. Commun. , 1824 (2002).

[26] B. Tian, X. Liu, B. Tu, C. Yu, J. Fan, L. Wang, S. Xie, G. D. Stucky, and D. Zhao, Nat. Mater. **2**, 159 (2003).

[27] G. J. de A. A. Soler-Illia and C. Sanchez, New. J. Chem. **24**, 493 (2000).

[28] F. A. Detcheverry, H. Kang, K. C. Daoulas, M. Müller, P. F. Nealey, and J. J. de Pablo, Macromolecules **41**, 4989 (2008).

[29] M. Müller, J. Stat. Phys. **145**, 967 (2011).

[30] M. Kallala, C. Sanchez, and B. Cabane, Phys. Rev. E **48**, 3692 (1993).

[31] J. Blanchard, F. Ribot, C. Sanchez, P.-V. Bellot, and A. Trokiner, J. Non-Cryst. Solids **265**, 83 (2000).

[32] G. J. de A. A. Soler-Illia, A. Louis, and C. Sanchez, Chem. Mater. **14**, 750 (2002).

[33] M. Müller and K. C. Daoulas, J. Chem. Phys. **129**, 164906 (2008).

[34] J. Schefer, R. McDaniel, and B. P. Schoenborn, J. Phys. Chem. **92**, 729 (1988).

[35] X.-Z. Cao, H. Merlitz, C.-X. Wu, and J.-U. Sommer, Phys. Rev. E **84**, 041802 (2011).

[36] X.-Z. Cao, H. Merlitz, C.-X. Wu, S. A. Egorov, and J.-U. Sommer, Soft Matter **9**, 5916 (2013).

[37] J. F. Joanny, L. Leibler, and P. G. de Gennes, J. Polym. Sci. B: Polym. Phys. **17**, 1073 (1979).

[38] M. Doxastakis, Y.-L. Chen, O. Guzmán, and J. J. de Pablo, J. Chem. Phys. **120**, 9335 (2004).

Physical Chemistry Chemical Physics Accepted Manuscript

[39] S. A. Bagshaw, Chem. Commun. , 271 (1999).

[40] F. Cagnol, D. Grosso, G. J. de A. A. Soler-Illia, E. L. Crepaldi, F. Babonneau, H. Amenitsch, and C. Sanchez, J. Mater. Chem. **13**, 61 (2003).

[41] S. M. Auerbach, W. Fan, and P. A. Monson, Int. Rev. Phys. Chem. **34**, 35 (2014).

[42] L. Jin, S. M. Auerbach, and P. A. Monson, J. Chem. Phys. **134**, 134703 (2011).

[43] F. Devreux, J. P. Boilot, and F. Chaput, Phys. Rev. A **41**, 6901 (1990).

[44] L. Jin, S. M. Auerbach, and P. A. Monson, Langmuir **29**, 766 (2013).

[45] S. W. Boettcher, M. H. Bartl, J. G. Hu, and G. D. Stucky, J. Am. Chem. Soc. **127**, 9721 (2005).

[46] R. Shenhar, T. B. Norsten, and V. M. Rotello, Adv. Mater. **17**, 657 (2005).

[47] A. Haryono and W. H. Binder, Small **2**, 600 (2006).

[48] A. C. Balazs, T. Emrick, and T. P. Russell, Science **314**, 1107 (2006).

[49] B. Sarkar and P. Alexandridis, Prog. Polym. Sci. **40**, 33 (2015).

[50] S. Cheng, S.-J. Xie, J.-M. Y. Carrillo, B. Carroll, H. Martin, P.-F. Cao, M. D. Dadmum, B. G. Sumpter, V. N. Novikov, K. S. Schweizer, and A. P. Sokolov, ACS Nano **11**, 752 (2017).

[51] R. B. Thompson, V. V. Ginzburg, M. W. Matsen, and A. C. Balazs, Science **292**, 2469 (2001).

[52] S. W. Sides, B. J. Kim, E. J. Kramer, and G. H. Fredrickson, Phys. Rev. Lett. **96**, 250601 (2006).

[53] M. W. Matsen and R. B. Thompson, Macromolecules **41**, 1853 (2008).

[54] Q. Tang and Y. Ma, J. Phys. Chem. B **113**, 10117 (2009).

[55] S. Kumar, B. Benicewicz, R. Vaia, and K. Winey, Macromolecules **50**, 714 (2017).

[56] L. S. Shagolsem and J.-U. Sommer, Macromol. Theory Simul. **20**, 329 (2011).

[57] L. S. Shagolsem and J.-U. Sommer, Macromolecules **47**, 830 (2014).

[58] A. Zelcer and G. J. A. A. Soler-Illia, J. Mater. Chem. C **1**, 1359 (2013).

[59] N. Tarutani, Y. Tokudome, M. Jobbágy, F. A. Viva, G. J. A. A. Soler-Illia, and M. Takahashi, Chem. Mater. **28**, 5606 (2016).
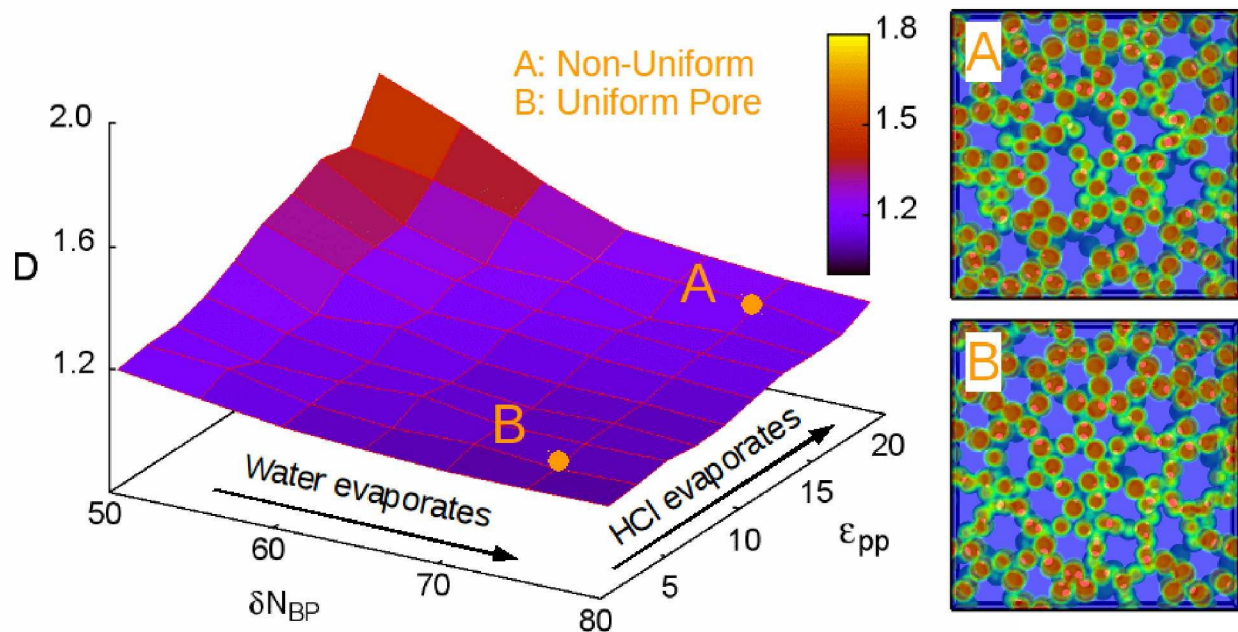
FIG. 10: Variation of the dispersity index D as water and HCl evaporate distinctly. Right panels show the snapshots of formed mesopores.